

Magnetoresistive sensors

To cite this article: P P Freitas *et al* 2007 *J. Phys.: Condens. Matter* **19** 165221

View the [article online](#) for updates and enhancements.

Related content

- [Topical Review](#)
Sarah M Thompson
- [Advances in magnetometry](#)
Alan Edelstein
- [Topical Review](#)
June W Lau and Justin M Shaw

Recent citations

- [High-Temperature Magnetic Tunnel Junction Magnetometers Based on \$\text{La}_{1-x}\text{Sr}_x\text{PtMn}\$ Pinned Layer](#)
Sina Ranjbar *et al*
- [Magnetic nanoparticles in microfluidic and sensing: From transport to detection](#)
Sumera Khizar *et al*
- [Miniaturized Magnetic Sensors for Implantable Magnetomyography](#)
Siming Zuo *et al*



IOP | ebooks™

Bringing together innovative digital publishing with leading authors from the global scientific community.

Start exploring the collection—download the first chapter of every title for free.

Magnetoresistive sensors

P P Freitas, R Ferreira, S Cardoso and F Cardoso

Instituto de Engenharia de Sistemas de Computadores–Microsystems and Nanotechnology (INESC–MN), Rua Alves Redol, n°9–1°, 1000-029 Lisboa, Portugal
and
Instituto Superior Técnico (IST), Physics Department, Avenida Rovisco Pais, 1096 Lisboa, Portugal

E-mail: pfreitas@inesc-mn.pt

Received 4 October 2006, in final form 9 February 2007

Published 6 April 2007

Online at stacks.iop.org/JPhysCM/19/165221

Abstract

Magnetoresistive sensors using spin valves and magnetic tunnel junctions are reviewed, considering applications as readers in hard disk drives, as well as applications where the ultimate field detection limits are required (from nT down to pT). The sensor noise level in quasi-DC or high-frequency applications is described, leading to sensor design considerations concerning biomedical and read head applications. Magnetic tunnel junction based sensors using MgO barriers appear as the best candidates for ultra-low field (pT) detection, either in the high-frequency regime, or for quasi-DC applications.

(Some figures in this article are in colour only in the electronic version)

1. Introduction

Magnetoresistive (MR) sensors are linear magnetic field transducers based either on the intrinsic magnetoresistance of the ferromagnetic material (sensors based on the spontaneous resistance anisotropy in 3d ferromagnetic alloys, also called anisotropic magnetoresistance (AMR) sensors), or on ferromagnetic/non-magnetic heterostructures (giant magnetoresistance multilayers, spin valve and tunnelling magnetoresistance (TMR) devices). This chapter covers spin valve (SV) and magnetic tunnel junction (MTJ) magnetoresistive sensors. The major present application of MR sensors is for the data storage market, as read heads in hard disk drives. AMR-based read heads replaced inductive readers in the early nineties, spin valve sensors entered the market in 1995–1996 and MTJ-based readers have been used since 2005. Magnetoresistive sensors find also applications in the automotive market (ABS sensors). The ability of magnetoresistive sensors to detect very weak magnetic fields (nT) at room temperature is being used in a growing number of new applications other than recording. Magnetoresistive biochips used for biomolecular recognition have emerged as an application with the potential to detect single molecule recognition processes. The optimization of sensor features in order to maximize the ultimate field detection limits are discussed considering the noise characteristics of the magnetoresistive sensors.

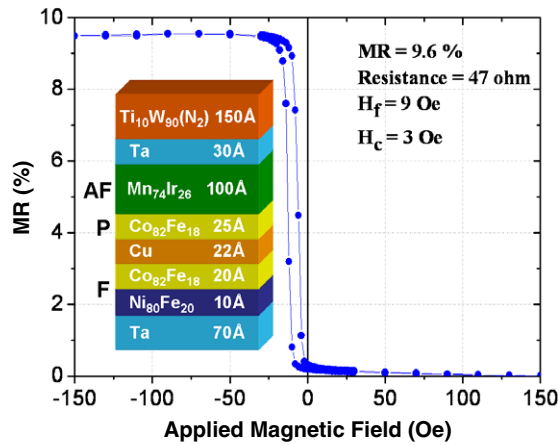


Figure 1. Magnetoresistance versus magnetic field for a top-pinned spin valve coupon sample. (P) pinned, (F) free, and (AF) antiferromagnetic layers.

2. Materials

2.1. Spin valves

Spin valves were introduced in 1991 [1], the first sensors were designed and tested in 1993–1994 [2, 3], and the first head prototypes were presented in 1994 [4]. A good review of the spin valve mechanism is given in [5]. Spin valves are based on the giant magnetoresistance effect (GMR) [6], and they rapidly replaced anisotropic magnetoresistance based read head sensors [7]. The GMR effect arises from the asymmetry in the spin-dependent scattering at the non-magnetic/magnetic interfaces for spin-up and spin-down electrons. When the magnetic layers have parallel magnetization directions, spin-up conduction electrons will be weakly scattered, and spin-down electrons will be strongly scattered. The spin-up channel will short the current leading to a low-resistance state. When the magnetic layers have antiparallel magnetization directions, both spin-up and spin-down electrons will alternatively be strongly and weakly scattered, leading to a high-resistance state.

Contrary to GMR multilayers, where the magnetization direction depends on the non-magnetic (Cu, Ru,...) spacer thickness leading to oscillatory coupling [6], in spin valves, one layer is engineered to have its magnetization pinned by exchange to an antiferromagnet [8], while the other is free to rotate. A typical spin valve structure consists then of two ferromagnetic layers, separated by a Cu spacer (figure 1). The buffer layer (Ta in this case) is chosen in order to provide a $\langle 111 \rangle$ texture, and control grain size to 10 nm leading to soft free layer properties. With Ta buffers, typical MR values up to 10% are obtained, (figure 1, top-pinned, MnIr-based spin valve, INESC-MN). The magnetoresistance dependence on the different layer thicknesses has been modelled in the semi-classical Boltzmann equation model [9]. The MR increases strongly by minimizing Cu thickness down to the continuity level of the Cu layer (15–18 Å, on Ta buffers). However, a decrease in Cu thickness leads to an increase in interlayer ferromagnetic Néel coupling, so a compromise is usually found near 20–22 Å Cu. Within the Boltzmann equation model, the MR dependence on ferromagnetic layer thickness depends on the interfacial transmission coefficients at the Cu/F interfaces, and on the spin-dependent bulk mean free paths in the ferromagnetic layer. Depending on ferromagnetic material (Co₉₀Fe₁₀, Ni₈₁Fe₁₉, Fe), maximum MR occurs for a ferromagnetic layer thickness varying from 60 Å down to 35 Å [5].

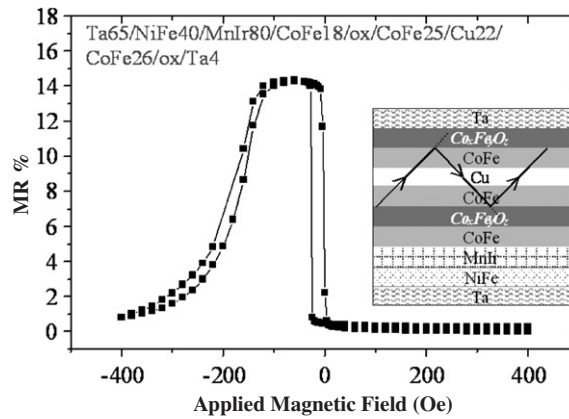


Figure 2. Magnetoresistance versus applied field for a specular spin valve coupon sample with two nano-oxide layers [13].

Further improvements on the MR ratio of current in plane (CIP) spin valves were obtained by changing from Ta buffers into $(\text{Ni}_{81}\text{Fe}_{19})_{60}\text{Cr}_{40}$ buffers [10]. The use of NiFeCr buffers dates back to the anisotropic magnetoresistance sensor days, where it was shown that NiFeCr can be made smoother than Ta (about 2 Å rms) achieving a higher degree of specularity at the NiFeCr/NiFe interface and leading to larger grain size, and therefore reducing grain boundary scattering and improving the AMR [5]. The arguments that led to larger AMR also lead to larger MR in the NiFeCr-based spin valve structures. MR values up to 15% were reported by different groups [10].

To further maximize the MR ratio, CIP spin valves can be made to incorporate nano-oxide layers (NOLs) to further confine the electron path within the active F/Cu/F layers (figure 2), and therefore reducing shunting effects and increasing specular reflection [11–13]. NOL layers are introduced at the free layer/cap interface and in the middle of the pinned layer. Increasing specularity decreases the total spin valve resistivity, enhancing the MR ratio. Figure 2 shows enhanced magnetoresistance (about 14.5%) in specular spin valves with two NOLs grown on Ta buffers [13]. Optimized specular spin valves with NiFeCr buffers and dual NOLs have reached MR values of 18–20% [14].

For sensor applications, and apart from large MR values, the exchange field created at the pinned layer/exchange layer interface is important. The exchange energy should be large ($>0.2 \text{ erg cm}^{-2}$) such that the exchange field prevails against demagnetizing fields. The blocking temperature (temperature where the exchange field vanishes) should exceed 300 °C, to prevent accidental de-pinning of the pinned layer during sensor life. Another factor to take into account is the effective coupling field between the free and pinned layers [15], which should not exceed 10–20 Oe to allow for proper biasing (see the transfer curve in figure 1, with an effective coupling field of 9 Oe). This coupling arises from the competition between ferromagnetic Néel coupling [16] (caused by corrugated interface roughness), indirect RKKY-like oscillatory exchange coupling across the Cu spacer [17], and the coupled demagnetizing fields of both layers in patterned sensors [18].

Concerning exchange fields, most sensors use synthetic antiferromagnets to increase the exchange and improve the temperature dependence of the exchange field. The synthetic antiferromagnet (SAF) consists of two Co or CoFe layers with similar thickness strongly antiferromagnetically coupled through 0.5–0.7 nm Ru [19, 20]. To avoid a spin flop transition under an external transverse field [20], a conventional exchange layer must be coupled to

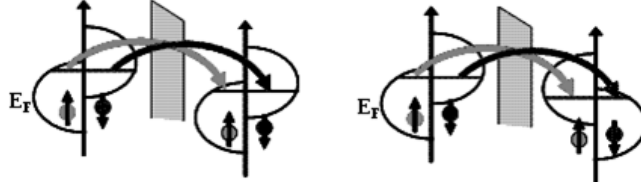


Figure 3. Schematic band structure for electrons tunnelling across the tunnelling barrier, in the parallel state (left) and antiparallel state (right).

one of the ferromagnetic layers. Although this strong AF coupling has a weak temperature dependence [22], this is not so for the conventional AF that must still have an optimum blocking temperature, but no longer large exchange. These SAF structures have another advantage. Since the effective moment of the pinned layer is low ($M_{\text{eff}} = M_1 - M_2$, where M_i is the moment of each ferromagnetic layer), its contribution to the demagnetizing and coupling fields acting on the free layer is much weaker than in conventional spin valves. Similar SAF structures can be used as synthetic free (SF) layers, in order to reduce the effective magnetic thickness and moment of the free layer [23, 24].

2.2. Magnetic tunnel junctions

In the spin-dependent tunnelling effect, electrons tunnel across an insulating barrier between two ferromagnetic electrodes [25]. Figure 3 shows the simplified band structure for the electrons involved in the tunnelling process. The tunnelling can be either incoherent (for example across an amorphous AlO_x barrier) or coherent (across a crystalline MgO barrier). For incoherent scattering (Julliere's model [26]), the tunnel magnetoresistance of such a junction is proportional to the product of both electrode polarizations P .

$$\text{TMR} = 2P_1 P_2 / (1 - P_1 P_2) \quad (1)$$

where

$$P_i = (D_{\uparrow}(\varepsilon_F) - D_{\downarrow}(\varepsilon_F)) / (D_{\uparrow}(\varepsilon_F) + D_{\downarrow}(\varepsilon_F)) \quad (2)$$

and where $D(\varepsilon_F)$ is the interfacial density of states at the Fermi level for the particular spin-up or spin-down bands.

Equations (1) and (2) lead to a low-resistance state when the two electrode magnetizations are in the parallel state, and a high-resistance state when they are in the antiparallel state. A typical magnetic tunnel junction has a structure similar to a spin valve, but with Cu replaced by the insulating barrier, and the current flowing from one electrode, across the barrier, into the other electrode. Figure 4 shows a 40% resistance change obtained upon free layer reversal, for a medium resistance, top-pinned, AlO_x tunnel barrier (Ta 50 Å/NiFe 70 Å/CoFe 20 Å/ AlO_x 15 Å/CoFe 25 Å/MnIr 100 Å/Ta 50 Å).

The interfacial spin polarization involved in the tunnelling process depends both on the ferromagnetic electrode and on the oxide barrier. Although known since the mid-1960s, only in the late 1990s have significant room-temperature TMR signals been observed [25, 27–31] (TMR up to 70% with amorphous AlO_x barriers). In 2004, TMR over 200% was reported for coherent tunnelling in crystalline fcc $\langle 100 \rangle$ MgO barriers [32, 33]. In most of these studies, transition metal ferromagnetic electrodes are used (CoFe, CoFeB, Fe). These results opened a realm of practical applications, among which, two of the most important are non-volatile magnetic tunnel junction random access memories (MRAM) and spin tunnel read heads. Figure 5 shows the minor-loop tunnel magnetoresistance for an MgO magnetic tunnel

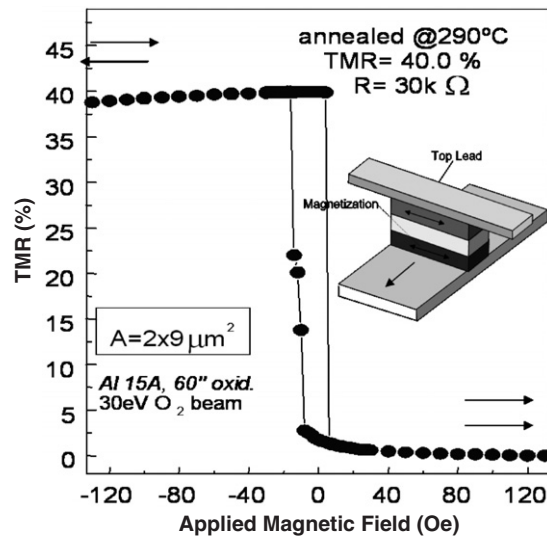


Figure 4. Minor-loop tunnel magnetoresistance (free layer reversal) for a $2 \times 9 \mu\text{m}^2$ tunnel junction [28].

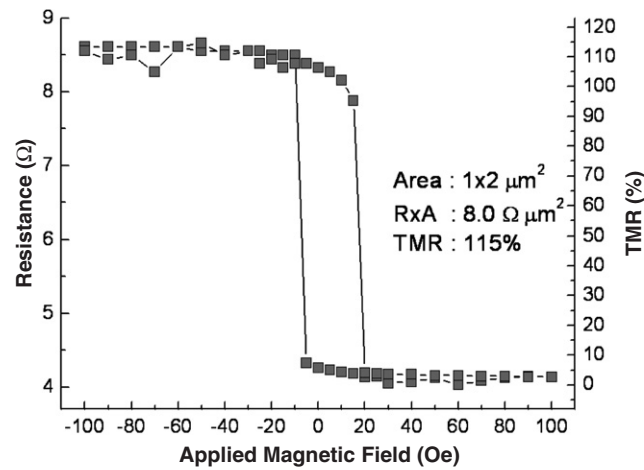


Figure 5. Minor-loop tunnel magnetoresistance (free layer reversal) for a $2 \times 1 \mu\text{m}^2$ MgO-based tunnel junction.

junctions with structure Ta 30 Å/CuN 300 Å/Ta 50 Å/PtMn 200 Å/CoFe 25 Å/Ru 7 Å/CoFeB 30 Å/MgO 12 Å/CoFeB 30 Å/Ta 50 Å (Singulus and INESC-MN [78, 79]).

3. Magnetoresistive sensors

3.1. Spin valve sensors

Depending on applications, the free and pinned layer easy axis of spin valves and magnetic tunnel junctions can be set either parallel (MRAM applications) or orthogonal (linear sensors, read heads), by controlling the magnetic field direction during deposition (induced magnetic anisotropy). For sensor applications the sensor output must be linearized. This can easily be achieved by inducing a transverse magnetization direction in the pinned layer, while the free

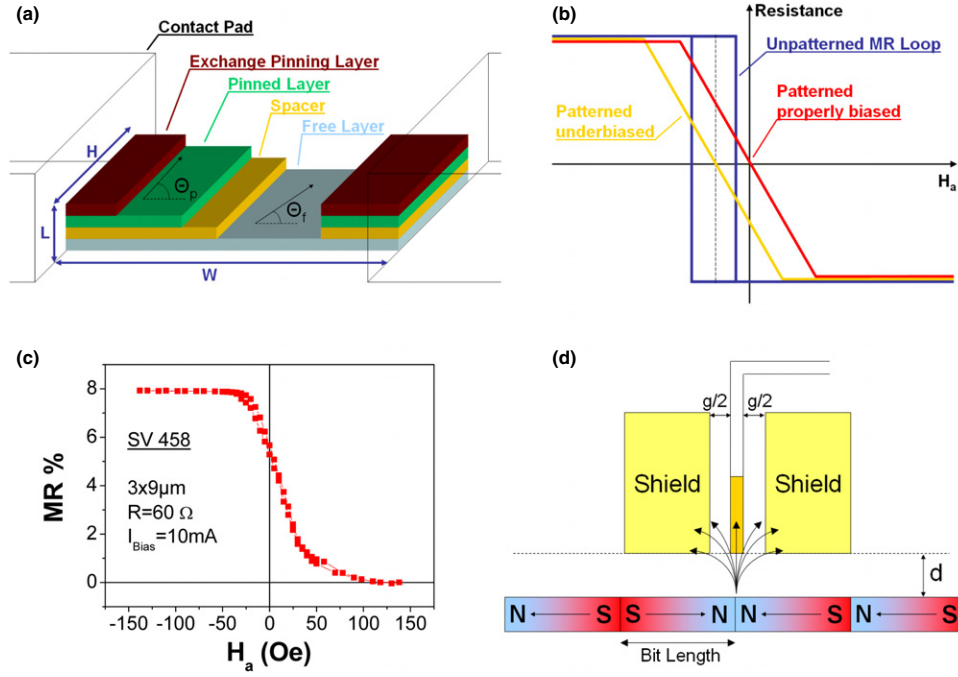


Figure 6. Spin valve sensors: (a) unshielded spin valve sensor schematics, (b) linearized transfer curve for the underbiased, and properly biased sensor, (c) experimental transfer curve for an unshielded spin valve sensor (INESC-MN), and (d) shielded spin valve sensor used as a read head.

layer, in its quiescent state, is in the longitudinal direction. Figure 6(a) shows an unshielded spin valve sensor with pinned and free layers at 90° (sensor or head applications) [2, 18]. Equation (3) gives the unshielded spin valve sensor output voltage.

$$\Delta V = \frac{1}{2}(\Delta R/R)R_{sq}I(W/h)(\cos(\Theta_f - \Theta_p)). \quad (3)$$

Here, $\Delta R/R$ is the maximum MR signal of the spin valve sensor (reaching nowadays 15–20% in specular spin valves), R_{sq} is the sensor square resistance ($R_{sq} = \rho/t = 15\text{--}20 \Omega/\text{sq}$), W the width of the read element (distance between leads), h is the sensor height, I the sensor current, Θ_f is the angle between the free layer magnetization and the longitudinal direction, Θ_p the angle between the pinned layer magnetization and the longitudinal direction, ρ is the sample resistivity, and t its thickness. The average $\langle \cdot \cdot \cdot \rangle$ is taken over the active area of the sensor (between leads). For linearized output ($\Theta_p = \pi/2$ and $\Theta_f \sim 0$). For the simple case where $W \gg h$, and assuming uniform magnetization for the free and pinned layers, $\langle \sin \Theta_f \rangle = (H_a + H_{bias} + H_{coupling})/H_{keff}$, where H_a is the external applied field and $H_{keff} = H_k + H_{demag}$. H_{keff} is the effective anisotropy field, incorporating the free layer shape anisotropy field (H_{demag}) and its uniaxial anisotropy field (H_k). H_{bias} is the bias field used to center the transfer curve [18]. $H_{coupling}$ corresponds to the sum of the ferromagnetic Néel coupling between the free and pinned layers, with the magnetostatic field coupling between the pinned and free layers. Equation (3) can then be rewritten as

$$\Delta V = (\Delta R/R)R_{sq}I(W/h)(H_a + H_{bias} + H_{coupling})/2H_{keff}. \quad (4)$$

Figure 6(b) shows the schematic transfer curve for an unpatterned spin valve coupon sample, and the linearized transfer curve for the underbiased, and properly biased (centred) patterned

sensor [18]. Figure 6(c) shows the experimental transfer curve for an unshielded spin valve sensor ($W = 6 \mu\text{m}$, $h = 2 \mu\text{m}$). Unshielded sensors are used in a variety of applications, normally in a Wheatstone bridge arrangement. For read head applications, the sensor is placed in between soft magnetic shields to increase response to the signal fields immediately below the magnetoresistive sensor.

For standard (non-NOL) spin valves, the longitudinal sense current through the sample provides the easiest way to bias the sensor. The thickness of the pinned and free layers can remain optimized for the MR signal, and the Néel plus magnetostatic field offset is corrected by the sense current bias field ($H_b(j)$). For NOL-containing spin valve structures, this sense current bias field can be strongly reduced in view of the reduced spatial current distribution in the spin valve, and the transfer curve offset must be corrected directly by controlling the pinned layer thickness or magnetization (the use of SAF pinned layer structures is in this case convenient) [34]. An alternative way of biasing the sensor is to use on-stack magnetostatic bias [35]. In this case, an extra hard layer is placed in the stack, creating an extra magnetostatic field that helps in linearizing the sensor.

For a shielded spin valve sensor used as a CIP read head, as in figure 6(d), the head output is given by equation (3) but now with $\langle \cos(\Theta_f - \Theta_p) \rangle = E \cdot \phi_{\text{ABS}} / tW\mu_0 M_s$,

$$\Delta V_{0-p} = (\Delta R/R) R_{\text{sq}} I W E \phi_{\text{ABS}} / 2tW\mu_0 M_s h \quad (5)$$

in SI units [36]. Here, ϕ_{ABS} is the media flux entering the shielded sensor at the head air bearing surface. The media flux leakage to the shields is described by the head efficiency $E = \tanh(h/2l_c)/(h/l_c)$, with l_c , the flux propagation length, defined as $l_c = (t\mu g_R/2)^{1/2}$, with μ the relative free layer permeability, M_s the free layer saturation magnetization, g_R the shield to sensor separation (read half gap), and t the free layer thickness [37].

CIP (current in plane) spin valve sensor read heads have reached a practical limit near 100 Gbit in^{-2} [38] since the spin valve MR ratio has been essentially unchanged topping 15%–20%, and further reductions in read gap (below 20 nm) are not possible in the sensor in gap geometry. Two alternatives appeared for new-generation read heads: CPP (current parallel to plane) read heads, either CPP spin valves or magnetic tunnel junctions. Both offer reduced shield to shield spacing (the current flows directly from shield to sensor) and therefore can immediately bring down the bit length, to the limit of the sensor thickness (30–40 nm). Heat dissipation is also improved and larger current densities can cross the CPP device improving the signal (CPP spin valves). In recent years, MTJ-based heads have come into production, since they offer large SNR advantages compared with CPP metallic stacks.

3.2. Magnetic tunnel junction sensors

Magnetoresistive sensors based on linear MTJs have a magnetic behaviour similar to spin valve sensors, but with quite higher MR ratios, and slightly higher noise levels. Figure 7 shows the MTJ transfer curve (R versus transverse applied field) at different external longitudinal biasing fields (0, 15 and 30 Oe), for an MTJ linear sensor [39]. The inset clarifies the sample geometry, easy axis directions defined during deposition, and transverse applied field and longitudinal bias field directions. From the hysteresis observed in the unbiased sample ($H_{\text{bias}} = 0 \text{ Oe}$), it is clearly seen that shape anisotropy only is not effective in fully linearizing the sensor. The help of a 15 Oe longitudinal bias is required at the expense of a decrease in sensitivity. In tunnel junction sensors, the sense current cannot be used for free layer biasing due to its circumferential symmetry. In this case, in-stack PM biasing or domain stabilization using particular free layer geometry is required. The MTJ sensor output is given by

$$\Delta V = (1/2) \text{TMR} I (RA/Wh) \langle \cos(\Theta_f - \Theta_p) \rangle. \quad (6)$$

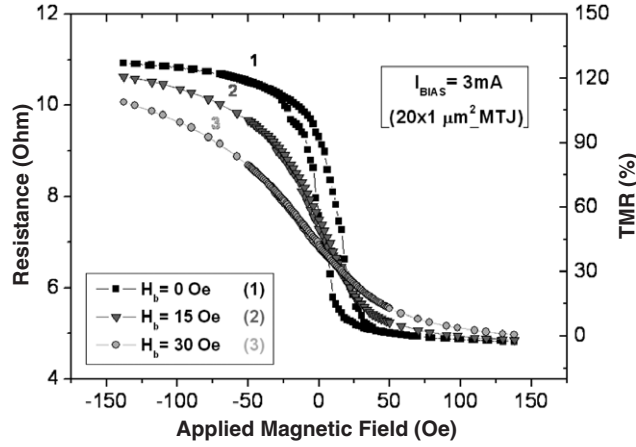


Figure 7. Transfer curves for a varying transverse field H_b are presented for the same junction. An increase in H_b leads to a decrease in the sensor sensitivity and the saturation also occurs at increasingly higher longitudinal fields.

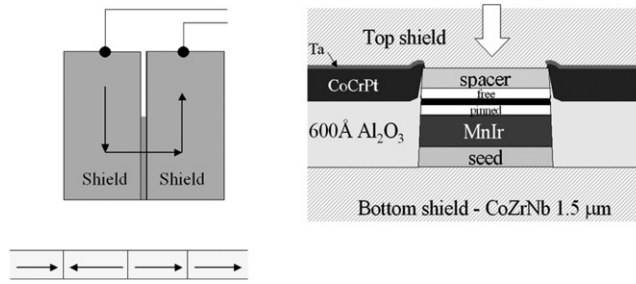


Figure 8. Tunnel junction head geometry developed at INESC-MN [40].

Here the tunnelling magnetoresistance depends on the bias voltage applied to the junction, in fact decreasing the available TMR at zero bias voltage. As for spin valve sensors, $\langle \cos(\Theta_f - \Theta_p) \rangle$ can be expressed in terms of H_a , H coupling and H_{keff} . For read head applications, in the 100–300 Gbit in^{-2} region, the junction resistance must be around $1 \text{ } \Omega \text{ } \mu\text{m}^2$. This low-resistance level is required in order to keep the read element resistance $< 100 \text{ } \Omega$, for compatibility with head amplifiers. Figure 8(a) illustrates how the low RA tunnel junction is incorporated in a shielded read head. Figure 8(b) shows the tunnel junction head geometry for prototypes developed at INESC-MN [40]. In this CPP design, the MTJ is at the ABS, and contacts are made through the shields. Lateral permanent magnet hard bias is used. Notice the small lateral insulating layer preventing the permanent magnet from shorting the tunnel junction. Critical for tunnel head fabrication is controlling the lapping process into the read element. MTJ heads were brought into production in mid-2005 by Seagate, and they are gradually replacing spin valve based readers [41].

3.3. Signal-to-noise ratio in SVs and MTJs for read head applications

Although the TMR in MTJs is significantly higher than the MR in SVs, the intrinsic noise of an MTJ sensor is also higher than that of an SV. MTJs can only perform better than the SVs provided their signal-to-noise ratio (SNR) is higher. Presently, read head sensors operate at a

frequency close to 1 GHz. At this frequency the only sources of noise which are present are thermal noise and shot noise (in MTJs). Thermal noise [42–45], caused by the random thermal motion of electrons, is described by

$$S_V^{\text{Thermal}}(\text{V}^2/\text{Hz}) = 4k_B T R. \quad (7)$$

Here, k_B is the Boltzmann constant, T represents the temperature and R represents the resistance of the device being considered. Shot noise [46–48] arises in discontinuities in the conduction medium as a consequence of the discrete nature of the electrical charge and is described by expression (8), where e stands for the electron electrical charge and I is the current flowing through the device (for practical device operating temperatures).

$$S_V^{\text{Shot}}(\text{V}^2/\text{Hz}) = 2eIR^2. \quad (8)$$

The tunnel barrier of an MTJ is an example of a discontinuity in the conduction medium, which is why shot noise is found in MTJs but not in SVs or AMR sensors which are made of continuous metallic layers. At frequencies around 3–6 GHz, for present head materials and sensor dimensions [49] additional noise associated with resonant spin precession around the effective magnetic field is found. This subject is out of the scope of this text but information concerning this subject is provided in [49–53].

While operating below the resonant frequency, the signal-to-noise ratio of a magnetoresistive sensor is given by expression (9), where V_b is the sensor bias voltage and V_n is the average noise level.

$$\text{SNR} = (\Delta R/R)V_b/V_n. \quad (9)$$

In the case of an MTJ, the magnetoresistance ratio depends on the bias voltage. Assuming a linear decrease of TMR with bias voltage, the bias voltage dependence of the MTJ can be described by

$$\text{TMR}(V_b) = \text{TMR}_0 \left(1 - \frac{V_b}{2V_{1/2}}\right) = \text{TMR}_0 \frac{2V_{1/2} - RI_b}{2V_{1/2}}. \quad (10)$$

Here, TMR_0 is the low-bias TMR and $V_{1/2}$ is the voltage bias at which TMR is reduced to half of its zero-bias value. $V_{1/2}$ is in the 400–800 mV range, depending on the MTJ quality and RA product value. Introducing (7), (8) and (10) into expression (9), the SNR of an MTJ sensor is found (in the thermally dominated noise regime):

$$\begin{aligned} \text{SNR}_{\text{MTJ}} &= \text{TMR}(V_b) \frac{V_b}{\sqrt{4k_B T R \Delta f + 2eI_b R^2 \Delta f}} \\ &= \text{TMR}_0 \frac{2V_{1/2} - RI_b}{2V_{1/2}} \sqrt{\frac{RI_b^2}{4k_B T \Delta f + 2eI_b R \Delta f}}. \end{aligned} \quad (11)$$

While the bias voltage is small compared with $V_{1/2}$, expression (11) is dominated by the last term with the SNR increasing with $\sim\sqrt{I_b}$. As the current keeps increasing, so does the voltage across the MTJ, and eventually the TMR falls due to the second term in (11). The decrease of the TMR will oppose the previous effect and the rate of increase of the SNR with the bias current slows down until a maximum is reached. Eventually the TMR decreases with bias voltage becoming the dominant effect, and the SNR will also decrease.

As an example, figure 9 shows the noise level in units of field S_V^{MTJ} ($\text{T Hz}^{-0.5}$) for a set of MgO junctions with $\text{TMR} \sim 120\%$, RA product $\sim 10\text{--}30 \Omega \mu\text{m}^2$, $V_{1/2} \sim 250$ mV and areas between 1×1 and $3 \times 8 \mu\text{m}^2$. Rather than the simple model in expression (11), the data presented in figure 9 were calculated using the measured $\text{TMR}(R, I)$ extracted from the experimental I – V characteristic and TMR versus bias voltage curve. The noise level in units

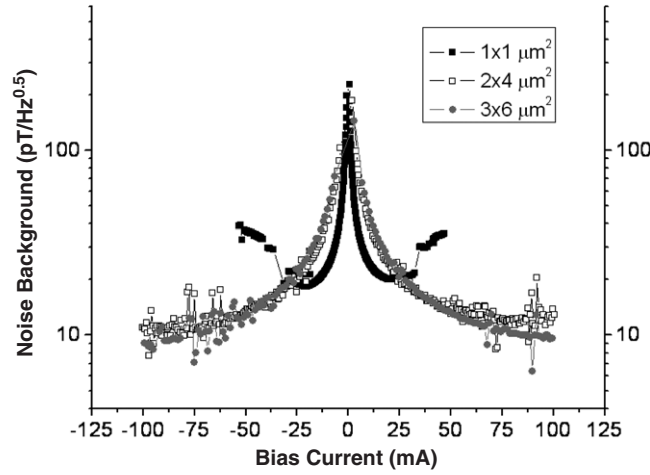


Figure 9. Noise background level of MgO MTJs (in magnetic field units) versus the bias current. A 30 Oe linear range was assumed. The noise background in units of field is proportional to $\sim 1/\text{SNR}$.

of field is inversely proportional to the SNR. Both figure 9 and formula (11) show that the bias current is a very important parameter in the determination of the SNR of an MTJ and it must be chosen with care.

In the case of a spin valve, there is no first-order dependence of the MR signal on the bias current and expression (9) simply becomes

$$\text{SNR}_{\text{SV}} = \text{MR} \frac{V_b}{\sqrt{4k_B T R \Delta f}} = \text{MR} \sqrt{\frac{R I_b^2}{4k_B T \Delta f}}. \quad (12)$$

For an SV sensor, the SNR is proportional to $\sim \sqrt{R I_b^2}$. Therefore the current used to bias the SV should be as high as possible, providing no excessive heating of the sensor occurs, and the transfer curve remains centred.

Taking sensor dimensions typical of 100 Gbit in^{-2} applications ($w = 100$ nm, $h = 120$ nm), an RA product of $2 \Omega \mu\text{m}^2$ for the MTJ ($R_{\text{MTJ}} = 167 \Omega$) and an R_{sq} of $20 \Omega/\text{sq}$ for the SV ($R_{\text{SV}} = 17 \Omega$) and taking $I_b = 1$ mA for the MTJ (the optimum bias for $V_{1/2} = 200$ mV) and $I_b = 3$ mA for the SV, the SNR for the two types of sensors can be compared:

$$\frac{\text{SNR}_{\text{MTJ}}}{\text{SNR}_{\text{SV}}} = 0.29 \frac{\text{TMR}}{\text{MR}}. \quad (13)$$

An MTJ sensor is advantageous over an SV sensor already at 100 Gbit in^{-2} provided that the TMR of the MTJ is 3.5 times larger than the MR of the SV.

4. Biomolecular recognition detection using magnetoresistive biochips: designing MR sensors for pT field detection

4.1. Overview

The ability of magnetoresistive sensors to detect weak magnetic fields is exploited in many different applications. A new and promising area concerns biomedicine and biotechnology. In the last decade, the detection of biomolecular recognition played an important role in areas such as health care, the pharmaceutical industry and environmental analysis.

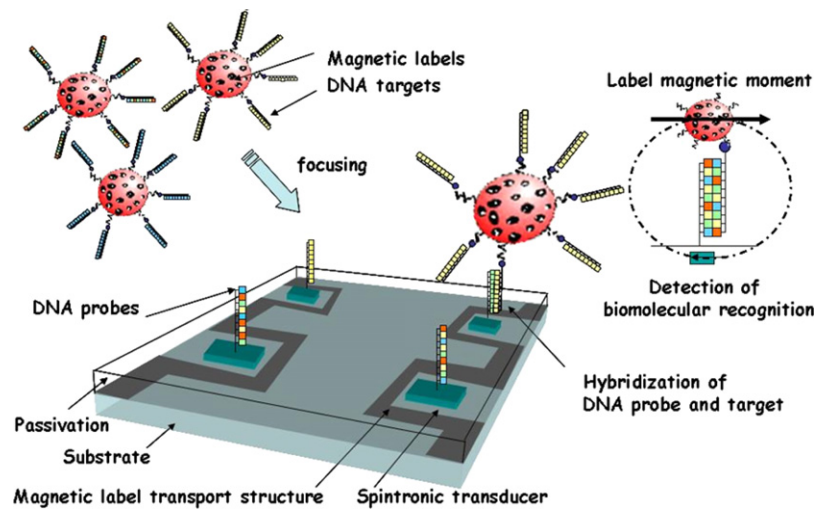


Figure 10. Example of biomolecular recognition assay using a magnetoresistive sensor (DNA hybridization example).

The main idea behind a magnetoresistive biochip is to provide a good alternative to traditionally used fluorescent marker devices. These devices use an expensive optical or laser-based fluorescence scanner system to detect fluorescent labelled biomolecules that recognized a known biomolecule previously immobilized on the sensor surface. In spintronic biochips, the fluorescent markers are replaced by magnetic nanoparticles and, in each probe, a magnetic sensor detects the stray field produced by the label giving an electrical signal. The advantages of this biochip are the fast response, the high sensitivity, the low background (since usually biological samples are non-magnetic), the ease of integration and automation.

A typical spintronic (or magnetoresistive) biochip consists of the following features (see figure 10).

- (i) An array of magnetoresistive sensors. On top of these sensors known biomolecules (such as gene-specific oligonucleotides or antibodies) are immobilized through microspotting, electrical or magnetic field arraying. These immobilized biomolecules are called probes.
- (ii) A hybridization chamber. Normally this chamber is based on microfluidic channel arrangements.
- (iii) A target arraying mechanism. This part consists of focusing the target elements on the probe sites. It can be done using an electric field for charged molecules (such as DNA), a magnetic field generating lines for targets labelled with magnetic particles, or simply be based on diffusion.

The targets are the biomolecules (DNA strand or antigens) that are to be detected. They are incubated in the chip for the biomolecular recognition to occur. The labelling of the targets can be executed before or after the recognition step. Typically, the magnetic labels are superparamagnetic or non-remnant ferromagnetic particles. These particles have micrometre or nanometre dimensions and can be attached to target biomolecules. Under a small magnetic field, these particles acquire a magnetic moment which produces a fringe field over the sensor. This induces a change in the magnetoresistive sensor resistance which is detected.

Magnetoresistive biochips were introduced by the Naval Research Laboratory group in 1998 [54]. At present, several sensor layouts and biochip prototypes have been fabricated. The

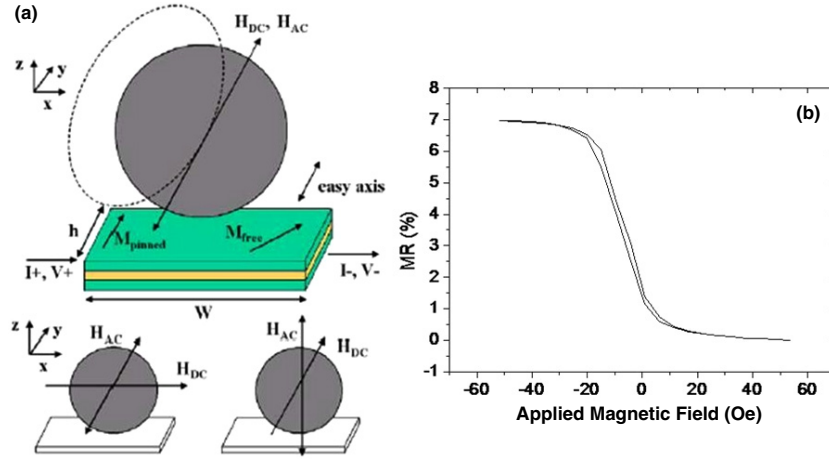


Figure 11. (a) Spin valve sensor. One of the detection modes uses an in-plane magnetic field in the sensing direction. (b) Sensor transfer curve.

various sensors reported for this application are:

- (i) anisotropic magnetoresistance (AMR) rings [55];
- (ii) planar Hall effect sensors [56, 57];
- (iii) GMR multilayer traces [58], serpentine [59] and spirals [60];
- (iv) spin valves [61–66];
- (v) magnetic tunnel junctions [67, 68].

Figure 11 shows the architecture of a standard biochip incorporating a spin valve as read element, and figure 12 shows the geometry of a biochip incorporating a tunnel junction as the read element. In this case, a thin film diode is incorporated in series with the MTJ, providing a way to select sensor sites out of a matrix of 16×16 sensors, as shown in figure 13.

Two concepts have to be introduced to design a magnetoresistive biochip: the biological sensitivity of the assay and the sensor label sensitivity. The biological sensitivity represents the capability of a biomolecule in solution to recognize its complementary biomolecule immobilized to the sensor surface. This parameter is increased with the increase of the functionalized area. Typically, DNA spots have a diameter of 50–100 μm , which means that the sensor should have the same sensing area in order to have a maximum signal.

The sensor label sensitivity is the capability for the sensor to detect a single magnetic particle. This capability, in turn, is limited only by the minimum field which the sensor can detect. As the magnetic particle fringe field is averaged over the sensor area, the increase of the sensor area comes with the decrease of the sensor label sensitivity. However, a larger sensor area increases the sensor dynamic range as the sensors are able to measure a larger number of particles. A smaller sensor area may be used to detect a smaller number of magnetic particles and at the limit this technology can be used for single biomolecular recognition events, such as the detection of a single DNA hybridization.

For spin valves and MTJs, the sensor output is that of equation (4) (or (6)) with H_a replaced by $\langle H_b \rangle$:

$$\text{Spin valve : } \Delta V = (1/2)(\Delta R/R)R_{\text{sq}}I(W/h)(H_{\text{bias}} + H_{\text{coupling}} + \langle H_b \rangle)/H_{\text{keff}} \quad (14)$$

$$\text{MTJ : } \Delta V = (1/2)\text{TMRI}(RA/Wh)(H_{\text{bias}} + H_{\text{coupling}} + \langle H_b \rangle)/H_{\text{keff}} \quad (15)$$

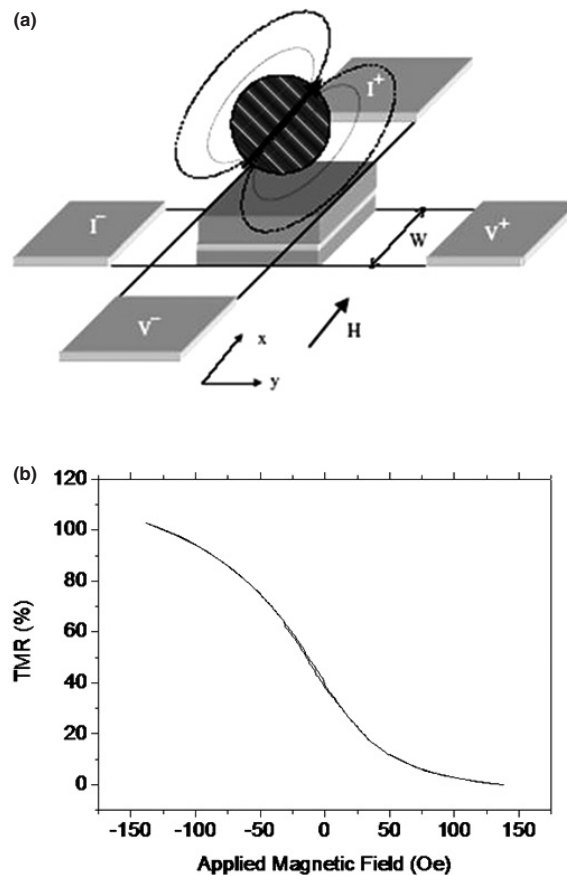


Figure 12. (a) Magnetic tunnel junction sensor with an MgO barrier. An in-plane DC or DC + AC field in the easy axis (EA) direction is applied to magnetize the particles. The sensor detects the particles' fringe field. (b) Sensor transfer curve with a 15 Oe bias field applied in the direction of the free layer magnetization.

where $\langle H_b \rangle$ is the averaged field of the magnetic particle over the sensor area. In summary, depending on the biochip application, the type of the sensor and its area may be optimized to detect either large concentrations of particles or single particles.

Several types of magnetic nanoparticle are used in biology and medicine (for cell separation, drug delivery...). In the case of magnetoresistive biochips, these magnetic particles are used to label the biomolecules and should have the following properties.

- (i) They have to be sufficiently small in such a way that they do not hinder the biomolecular processes (recognition, interaction...).
- (ii) They should have a non-remanent moment to reduce the particle coalescence due to the dipolar interaction between neighbouring particles.
- (iii) They should have a high magnetic moment under a magnetic field in order to have larger fringe fields to be detected by the sensor.

Having these characteristics in mind, usually superparamagnetic particles are chosen as labels for biological assays. This means that a magnetizing field has to be applied to magnetize the particles. This field can be a DC field, an AC field or a DC + AC field.

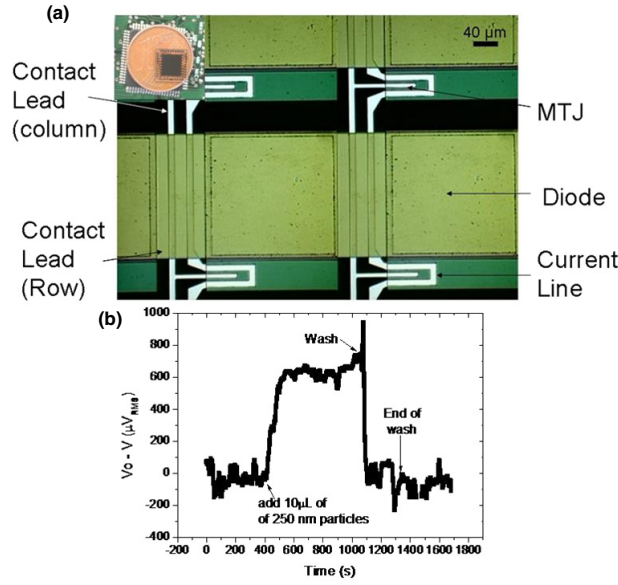


Figure 13. (a) Top view of four elements of a 16×16 matrix. Each element is surrounded by a U-shaped focusing line. (Inset: view of the full chip over a cent coin.) (b) Response of a matrix element to $10 \mu\text{l}$ of a 1:10 dilution (initial solution with ~ 1011 particles ml^{-1}) of 250 nm magnetic particles. An in-plane 6 Oe DC magnetic field and an in-plane 15 Oe rms magnetic field were used respectively to put the sensor in the most sensitive area and to magnetize the magnetic particles to have an AC measurement.

The magnetic particle is characterized by its susceptibility,

$$\mathbf{M} = \chi \mathbf{H}. \quad (16)$$

The fringe field of the particle created in the plane of the sensor, assuming that the magnetization of the particle along the transverse direction of the sensor is given by the following expression:

$$H_x(x, y, z) = (m_0/4\pi) \{ 3x^2/(x^2 + y^2 + z^2)^{5/2} - 1/(x^2 + y^2 + z^2)^{3/2} \} \quad (17)$$

where $m_0 = VM$ is the magnetic moment, V is the volume, and M the magnetization of the magnetic particle. The z direction is the out of plane direction while x and y are the directions transverse and longitudinal to the sensor, respectively (see figure 14). Table 1 shows the characteristics of several magnetic particles at a magnetizing field of 15 Oe and the expected maximum and average fringe field ($\langle B_b \rangle = \mu_0 \langle H_b \rangle$) created over a 2×6 and $2.5 \times 80 \mu\text{m}^2$ sensing layer.

4.2. Limits of detection

The reported measurements in these magnetoresistive biochips [54–69] were made at low frequencies (DC up to few kHz), normally in the $1/f$ dominated regime. While the white noise floor level of a sensor can be accurately calculated with expressions (7) and (8), the $1/f$ noise is described by phenomenological models with parameters that must be measured. In the case of a spin valve sensor [70–72], $1/f$ noise is well described by the following expression:

$$S_V^{1/f\text{SV}} (\text{V}^2/\text{Hz}) = \frac{\gamma I^2 R^2}{N_C f}. \quad (18)$$

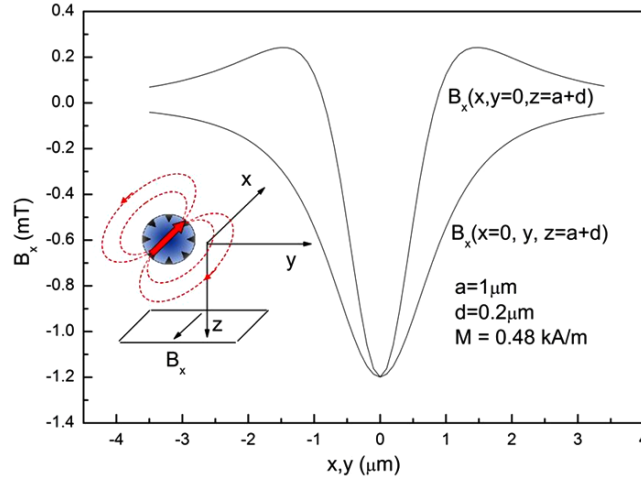


Figure 14. Transverse magnetic field created by a $2\ \mu\text{m}$ diameter particle at a distance $d = 0.2\ \mu\text{m}$. The magnetic particles have a magnetization $M = 0.48\ \text{kA m}^{-1}$.

Table 1. Examples of magnetic particle properties. The magnetization and magnetic moment were measured at a magnetizing field of $1.2\ \text{kA m}^{-1}$ (15 Oe). The B_{max} values were calculated using equation (17) with $x = y = 0$ and $z = 0.6\ \mu\text{m}$. The $\langle B_b \rangle$ were calculated using equation (17) and averaging the field of a single particle over the centre of the sensing area $6 \times 2\ \mu\text{m}^2$ and $80 \times 2.5\ \mu\text{m}^2$.

Diameter (nm)	Magnetization (magnetic moment) kA m^{-1} (emu)	B_{max} (T)	$\langle B_b \rangle$ over a $6 \times 2\ \mu\text{m}^2$ area (T)	$\langle B_b \rangle$ over a $80 \times 2.5\ \mu\text{m}^2$ area (T)
2800	0.40 (4.60×10^{-12})	-1.12×10^{-4}	0.37×10^{-4}	2.79×10^{-6}
2000	0.48 (2.01×10^{-12})	-1.16×10^{-4}	0.24×10^{-4}	1.67×10^{-6}
250	20.1 (1.64×10^{-13})	-4.79×10^{-4}	4.67×10^{-6}	2.46×10^{-7}
130	17.8 (2.05×10^{-14})	-1.10×10^{-4}	6.04×10^{-7}	3.14×10^{-8}
100	0.34 (1.78×10^{-16})	-1.14×10^{-6}	5.28×10^{-9}	2.74×10^{-10}
50	0.85 (5.56×10^{-17})	-4.88×10^{-7}	1.6×10^{-9}	8.61×10^{-11}

Here, f stands for the frequency, N_C is the number of current carriers participating in the current I and γ is the phenomenological Hooke parameter, which is a parameter quantifying the magnitude of the $1/f$ noise for a certain device. In the case of an MTJ [73–79], the $1/f$ noise is usually described by a slightly different expression more adequate to a CPP geometry, where A stands for the MTJ area and α_H is a modified Hooke parameter:

$$S_V^{1/f\text{MTJ}} (\text{V}^2/\text{Hz}) = \frac{\alpha_H I^2 R^2}{A f}. \quad (19)$$

Once the device noise spectral density is known, the magnitude of the Hooke parameter can be obtained by fitting the measured power density to expressions (18) or (19). Figure 15 shows the spectral noise density obtained for an MgO-based MTJ (TMR $\sim 120\%$ and RA product $\sim 30\ \Omega\ \mu\text{m}^2$) with bias currents going from 0 to 3 mA [79]. Fitting each measured curve to the expression (19) with the addition of the white noise background, the value of the Hooke parameter is found to be $\alpha_H = 1.24 \times 10^{-9}\ \mu\text{m}^2$. Data gathered from several groups [73–79] suggest that while the barrier material of the MTJ has no effect on the $1/f$ noise magnitude, the RA product of the MTJ is an important parameter. In the range

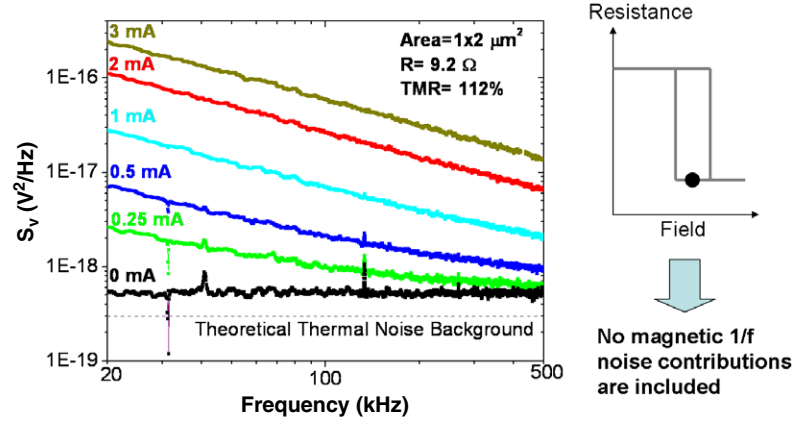


Figure 15. Noise spectrum density of an MgO MTJ as function of the bias current. The MTJs have parallel anisotropy easy axes. The measurement is made at zero magnetic field, in the minimum resistance saturation branch.

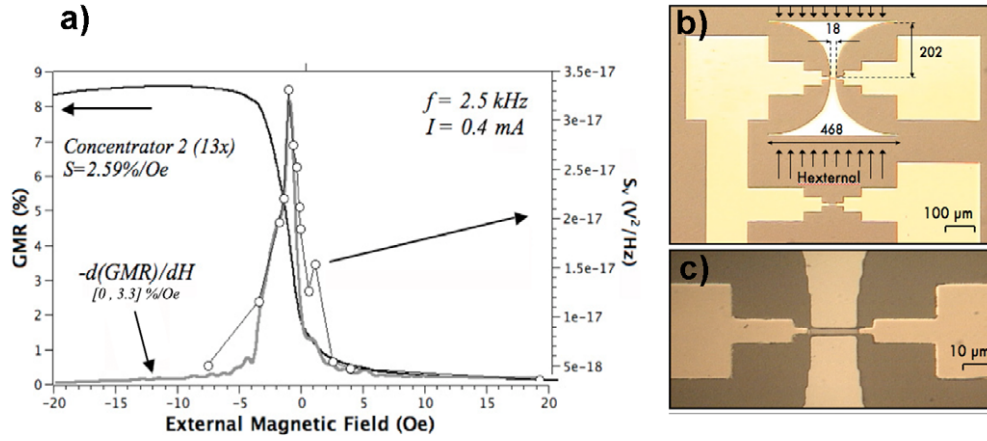


Figure 16. Noise spectral density measured for three different frequencies versus the applied magnetic field in a sensor with non-perfect monodomain free layer configuration. At low frequencies the noise in the active region of the sensor is about one order of magnitude higher with respect to saturation.

below $1 \text{ M}\Omega \mu\text{m}^2$ the Hooke parameter is in the $0.5 \times 10^{-9} \mu\text{m}^2$ to $2.0 \times 10^{-9} \mu\text{m}^2$ range. For RA product values above $1 \text{ M}\Omega \mu\text{m}^2$ new $1/f$ noise sources appear in the thick tunnel barriers and the Hooke parameter increases by orders of magnitude. The values of the Hooke parameter just reported apply to a saturated MTJ (no magnetic $1/f$ noise contribution). When measuring $1/f$ noise in linear sensors a new noise component becomes important: magnetic $1/f$ noise [64, 73, 74, 77, 78]. This can be seen in figure 16, where the noise spectral density at low frequencies is shown to display a significant increase in the linear range of the sensor with respect to saturation. Magnetic $1/f$ noise has its origin in fluctuations of the magnetic domains making up the free and pinned layer of the sensor. It has a magnitude proportional to the MR sensor transfer curve R versus H slope. The minimization of $1/f$ magnetic noise through the stabilization of the domain structure of the magnetic layers is a subject of active research.

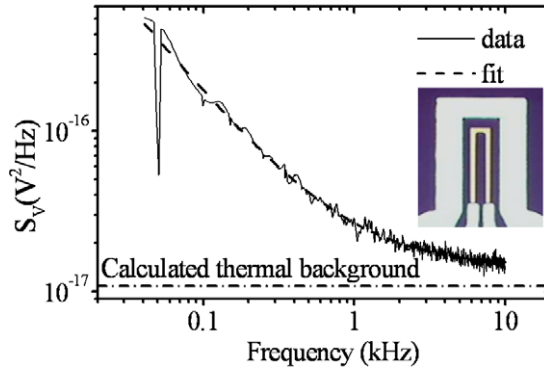


Figure 17. Noise spectra for a $2.5 \times 80 \mu\text{m}^2$ spin valve sensor in the linear regime with a resistance of $\sim 650 \Omega$ and a sense current of 0.1 mA. A fit is shown for the $1/f$ noise and thermal contributions, and the calculated thermal background is also displayed.

If a spin valve is used instead of an MTJ the procedure used to extract the Hooge parameter γ from the spectral noise density is essentially the same. In this case, however, the number of carriers must be estimated in order to extract γ . The procedure followed to calculate the number of charge carriers participating in the current basically consists in assigning one carrier per atom to each atom in the lowest resistance layers of the spin valve stack. It is a good approximation to consider that only the free layer, pinned layer and Cu spacer contribute with electrons to the current. A spin valve with the structure Ta 20 Å/Ni₈₀Fe₂₀ 30 Å/Co₈₁Fe₁₉ 25 Å/Cu 26 Å/Co₈₁Fe₁₉ 25 Å/Mn₇₆Ir₂₄ 60 Å/Ta 30 Å/Ti₁₀W₉₀N 150 Å and a sensing area of $2.5 \times 80 \mu\text{m}^2$ is estimated to have 2.48×10^{11} carriers, using the prescribed method. With this figure the Hooge parameter value extracted from a spin valve noise density spectrum, shown in figure 17, is $\gamma \sim 1$.

In order to compare SVs with MTJ-based sensors, it is convenient to express the noise in field units. The voltage fluctuations S_V ($\text{V Hz}^{-0.5}$) measured at a certain frequency f due to the noise in a linear magnetoresistive sensor correspond to a minimum field H_{\min} that could be detected by this sensor. Equation (20) expresses H_{\min} . Here, ΔR is the change in resistance between the two saturation states and ΔH is the linear range of the sensor.

$$H_{\min}(\text{T Hz}^{-0.5}) = S_V(\text{T Hz}^{-0.5}) = \frac{S_V(\text{V Hz}^{-0.5})}{I \frac{\Delta R}{\Delta H}}. \quad (20)$$

In the low-frequency limit the thermal noise and shot noise are negligible when compared to the $1/f$ noise. In the case of an MTJ expression (20) takes the form

$$S_V^{\text{MTJ}}(\text{T Hz}^{-0.5}) = \frac{\sqrt{\frac{\alpha_H I^2 R^2}{A f}}}{I \cdot \frac{\Delta R}{\Delta H}} = \frac{\Delta H}{\text{TMR}} \sqrt{\frac{\alpha_H}{A f}}. \quad (21)$$

In the case of an SV in the low-frequency limit, expression (20) takes the form

$$S_V^{\text{SV}}(\text{T Hz}^{-0.5}) = \frac{\sqrt{\frac{\gamma I^2 R^2}{N_C f}}}{I \cdot \frac{\Delta R}{\Delta H}} = \frac{\Delta H}{\text{MR}} \sqrt{\frac{\gamma}{N_C f}} = \frac{\Delta H}{\text{MR}} \sqrt{\frac{\gamma A_{\text{SV}}}{N_C A_{\text{SV}} f}}. \quad (22)$$

It is clear that the low-frequency limit depends on a very restricted number of parameters: linear range ΔH , MR or TMR depending on the device considered, Hooge parameter, frequency, and the number of carriers (SV) or area (MTJ). Notice that the bias current does not have any effect

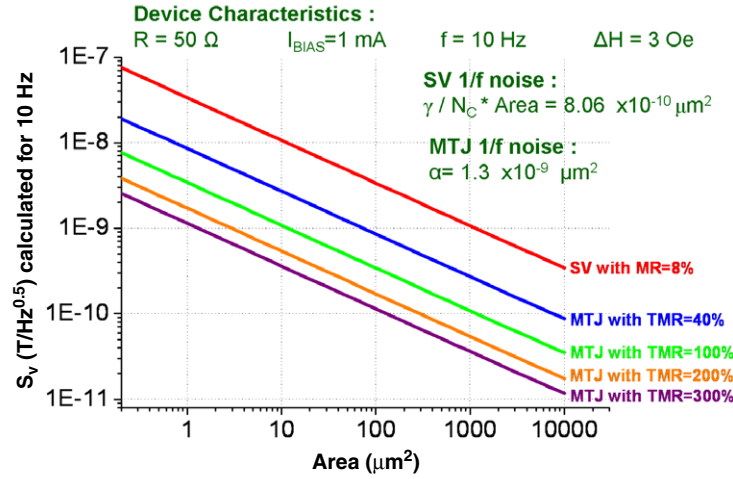


Figure 18. Magnetic field detection limits calculated at 10 Hz as a function of sensor area and magnetoresistance. No magnetic noise contribution was considered.

on the result (except for the TMR dependence on bias voltage) since both the signal and the noise are proportional to I . The same is true for the sensor resistance.

Comparing expression (21) with expression (22) it is clear that with the above assumptions $\gamma A_{SV}/N_C$ plays the same role as the MTJ α_H parameter. From the spin valve example previously given $\gamma A_{SV}/N_C$ can be computed. This parameter, which is constant for spin valves with a similar structure, has a value of $8.06 \times 10^{-10} \mu\text{m}^2$. We can now compare the minimum field detectable using an SV sensor with the minimum field detectable with an MTJ in the low-frequency limit. The ratio between expression (21) and (22) assuming that the MTJ and SV have the same area (and therefore the same spatial resolution), the same linear range and the same frequency of operation is computed below:

$$\frac{S_{1/f}^{\text{MTJ}} (\text{T Hz}^{-0.5})}{S_{1/f}^{\text{SV}} (\text{T Hz}^{-0.5})} = \frac{\text{MR}}{\text{TMR}} \sqrt{\frac{\alpha_H}{\gamma A_{SV}/N_C}}. \quad (23)$$

On the one hand, the weak field detection favours MTJ over SV sensors because of the MR/TMR term which compares the signal of the two sensor types. A typical SV has $\text{MR} \sim 8\%$ while a typical MgO-based MTJ can display $\text{TMR} \sim 200\text{--}350\%$. The first factor in expression (23) has therefore a value between 0.04 and 0.023. On the other hand, the second term of formula (23), which compares the noise in both sensors, favours the spin valve. Based on the measurements presented before, the value of $\sqrt{\frac{\alpha_H}{\gamma A_{SV}/N_C}}$ is somewhere between 1.27 in the most favourable situation for an MTJ (considering that the magnetic $1/f$ noise can be suppressed with $\alpha_H = 1.3 \times 10^{-9} \mu\text{m}^2$) and 4.01 in the most favourable situation for a spin valve (considering a magnetic $1/f$ noise contribution resulting in $\alpha_H = 1.3 \times 10^{-8} \mu\text{m}^2$). Both terms considered, an MTJ operating in the low-frequency limit should be able to detect a magnetic field between 10 and 20 times weaker than a spin valve with the same area, linear range and operating frequency. MTJs should therefore always be preferred over spin valves in the low-frequency limit. The only parameters that can be used to minimize $S_V^{\text{MTJ}} (\text{T Hz}^{-0.5})$ in expression (23) are the TMR, linear range and area. Figure 18 shows the calculated $S_V^{\text{MTJ}} (\text{T Hz}^{-0.5})$ for MgO MTJs as a function of sensor area for several values of magnetoresistance. A linear range of just 3 Oe was assumed, requiring the integration of flux guides in the sensor. Provided the TMR of the MTJs can be maintained over large areas, the

detection of fields as weak as $0.1 \text{ nT Hz}^{-0.5}$ should be possible even at a frequency of just 10 Hz.

Despite the ability of MTJs to detect weaker magnetic fields than SVs with similar electrical and geometrical properties, thus far systems using SVs for biomolecular recognition have outnumbered those with MTJs. There are mainly two reasons for the preference of SVs over MTJs.

The first reason concerns the microfabrication process. It is quite simple to manufacture CIP SVs, while CPP MTJs require more complicated processes. Unless the detection of very weak fields is required, the integration of an SV in a biochip is more effective than the integration of an MTJ.

The second reason concerns the need for MTJ optimization prior to integration in a biochip. Notice that the detection of fields of the order of $\sim 0.1 \text{ nT Hz}^{-0.5}$ requires MTJs with areas of $\sim 1000 \mu\text{m}^2$ while keeping a high TMR value. This seems a reasonable goal since TMR values of up to $\sim 225\%$ have been demonstrated in MgO MTJs manufactured with $80 \times 80 \mu\text{m}^2$ [32]. But according to the calculations, even lower fields can be detected for even larger junction areas. In practice the area of an MTJ cannot be arbitrarily large since for larger areas the probability of pinholes in the tunnelling barrier increases, resulting in reduced TMR. It is hard to specify a maximum limit for a junction area since this depends strongly on the manufacturing process and on the thickness and quality of the barrier. But it is important to stress that pinhole free barriers over large areas are a condition for the results in figure 18 to hold. This problem does not happen with spin valves, giving an advantage to this sensor type in applications where a large area is fundamental to increase the biological sensitivity (see section 4.2).

In conclusion, the choice between the MTJ and the spin valve sensor for magnetoresistive biochips applications depends on the biological sensitivity and on the number of labels to be detected required for a specific assay. In this choice, the signal to noise ratio of the sensor is a very important parameter but the absolute voltage variation is not less important. Finally, the experimental setup has to be designed so that it does not introduce more noise than the sensor in the measured values.

This article has shown that MR sensors alone can be fabricated that can detect fields down to 10 to 100 pT at quasi-DC frequencies. Further improvements in field detection can be accomplished with hybrid devices incorporating magnetic or superconducting static flux guides. $\text{fT Hz}^{-0.5}$ resolution has been achieved using standard spin valve sensors with superconducting ring flux guides [80]. Further improvement to sub-fT $\text{Hz}^{-0.5}$ detection should be possible by further eliminating the $1/f$ noise contribution. One possibility is to include an AC MEMS structure that modulates the DC signal field to a frequency above the $1/f$ knee [81]. These fT detection capabilities will open new MR sensor applications in the biomedical imaging arena.

References

- [1] Dieny B, Speriosu V S, Parkin S S, Gurney B A, Wilhoit D R and Mauri D 1991 *Phys. Rev. B* **43** 1297
- [2] Heim D E, Fontana R E, Tsang C, Speriosu V S, Gurney B A and Williams M L 1994 *IEEE Trans. Magn.* **30** 316
- [3] Freitas P P, Leal J L, Melo L V, Oliveira N J, Rodrigues L and Sousa A T 1994 *Appl. Phys. Lett.* **65** 493
- [4] Tsang C, Fontana R E, Lin T, Heim D E, Speriosu V S, Gurney B A and Williams M L 1994 *IEEE Trans. Magn.* **30** 3801
- [5] Dieny B 2004 Spin Valves in *Magnetoelectronics* ed M Johnson (Amsterdam: Elsevier)
- [6] Baibich M, Broto J M, Fert A, Nguyen Van Dau F, Petroff F, Etienne P, Creuzet G, Friederich A and Chazelas J 1988 *Phys. Rev. Lett.* **61** 2472
- [7] Smith N 1987 *IEEE Trans. Magn.* **23** 259
- [8] Lederman M 1999 *IEEE Trans. Magn.* **35** 794

- [9] Dieny B 1992 *J. Phys.: Condens. Matter* **4** 8009
- [10] Lee Ch-L, Devasahayam A J, Hu C-C, Zhang Y, Mao M, Kools J C S and Rook K 2004 *IEEE Trans. Magn.* **40** 2209
- [11] Kamiguchi Y, Yuasa H, Fukuzawa H, Kouji K, Iwasaki H and Sahashi M 1999 *Digest DB-01, INTERMAG (Korea, 1999)*
- [12] Sakakima H, Satomi M, Sugita Y and Kawawake Y 2000 *J. Magn. Magn. Mater.* **210** L20
- [13] Veloso A, Freitas P P, Wei P, Barradas N P, Soares J C, Almeida B and Sousa J B 2000 *Appl. Phys. Lett.* **77** 1020
- [14] Hasegawa N, Koile F, Ikarashi K, Ishizone M, Lawamura M, Nakazawa Y and Takahashi A 2002 *J. Appl. Phys.* **91** 8774
- [15] Kools J C S, Rijkers Th G S M, de Veirman A E M and Coehoorn R 1995 *IEEE Trans. Magn.* **31** 3918
- [16] Néel L 1962 *C. R. Acad. Sci.* **255** 1545
- [17] Bruno P and Chappert C 1991 *Phys. Rev. Lett.* **67** 1602
- [18] Albuquerque G B and Freitas P P 1997 *Physica B* **233** 294
- [19] Coffey K R, Gurney B A, Heim D E, Lefakis H, Mauri D, Speriosu V S and Wilhoit D R 1996 *US Patent Specification* 5583725, 10 December 1996
- [20] van den Berg H, Clemens W, Gieres G, Rupp G, Schelter W and Vieth M 1996 *IEEE Trans. Magn.* **32** 4624
- [21] Zhu J G 1999 *IEEE Trans. Magn.* **35** 655
- [22] Leal J L and Kryder M 1999 *IEEE Trans. Magn.* **35** 800
- [23] Veloso A and Freitas P P 2000 *J. Appl. Phys.* **87** 5744
- [24] Veloso A, Dee R H and Freitas P P 2002 *IEEE Trans. Magn.* **38** 1928
- [25] Moodera J, Nassar J and Mathon G 1999 *Annu. Rev. Mater. Sci.* **29** 381
- [26] Julliere M 1975 *Phys. Lett. A* **54** 225
- [27] Parkin S S, Roche K P, Samant M G, Rice P M, Beyers R B, Scheurlein R E, O'Sullivan E J, Brown S L, Bucchiganno J, Abraham D W, Lu Y, Rooks M, Trouiloud P L, Wanner R A and Gallagher W J 1999 *J. Appl. Phys.* **85** 5828
- [28] Sousa R C, Sun J J, Soares V, Freitas P P, Kling A, daSilva M F and Soares J C 1998 *Appl. Phys. Lett.* **73** 3288
- [29] Cardoso S, Gehanno V, Ferreira R and Freitas P P 1999 *IEEE Trans. Magn.* **35** 2952
- [30] Zhang Z-Zh, Cardoso S, Freitas P P, Battle X, Wei P, Barradas N and Soares J C 2001 *J. Appl. Phys.* **89** 6665
- [31] Wang D, Nordman J, Daughton J M, Qian Z and Fink J 2004 *IEEE Trans. Magn.* **40** 2269
- [32] Parkin S, Kaiser C, Panchula A, Rice P, Hughes B, Samant M and Yang S 2004 *Nat. Mater.* **3** 862
- [33] Yuasa S, Nagahama T, Fukushima A, Suzuki Y and Ando K 2004 *Nat. Mater.* **3** 868
- [34] Guedes A, Mendes M J, Freitas P P and Martins J L 2006 *J. Appl. Phys.* **99** (April) 08B703–5
- [35] Childress J, Ho M K, Fontana R E, Carey M J, Rice P M, Gurney B A and Tsang C H 2002 *IEEE Trans. Magn.* **38** 2286
- [36] Bertram H N 1995 *IEEE Trans. Magn.* **31** 2573
- [37] Mee C D and Daniel E D 1995 *Magnetic Recording Technology* (New York: McGraw-Hill) p 6.45
- [38] Hong J, Hashimoto J, Yamagishi M, Noma K and Kanai H 2002 *IEEE Trans. Magn.* **38** 15
- [39] Almeida J M, Ferreira R, Freitas P P, Langer J, Ocker B and Maass W 2006 *J. Appl. Phys.* **99** 08B314
- [40] Freitas P P, Cardoso S, Sousa R, Ku W, Ferreira R, Chu V and Conde J P 2000 *IEEE Trans. Magn.* **36** 2796
- [41] Mao S-N, Nowak J, Song D, Kolbo P, Wang L, Linville E, Saunders D, Murdock E and Ryan P 2002 *IEEE Trans. Magn.* **38** 78
- [42] Johnson J B 1927 *Nature* **119** 50
- [43] Johnson J B 1927 *Phys. Rev.* **29** 367
- [44] Nyquist H 1928 *Phys. Rev.* **32** 110
- [45] Lecoy G and Gousskov L 1968 *Phys. Status Solidi* **30** 9
- [46] Nowak E R, Weissman M B and Parkin S S P 1999 *Appl. Phys. Lett.* **74** 600
- [47] Schottky W 1918 *Ann. Phys., Lpz.* **57** 541
- [48] Klaassen K B, van Peppen J C L and Xing X 2003 *J. Appl. Phys.* **93** 8573
- [49] Klaassen K B, Xing X and Peppen J C L 2005 *IEEE Trans. Magn.* **41** 2307
- [50] Smith N and Arnett P 2001 *Appl. Phys. Lett.* **78** 1448
- [51] Smith N 2001 *J. Appl. Phys.* **90** 5768
- [52] Stutzke N, Burkett S L and Russek S E 2003 *Appl. Phys. Lett.* **82** 91
- [53] Jury J C, Klaassen K B, Peppen J C L and Wang S X 2002 *IEEE Trans. Magn.* **38** 3545
- [54] Baselt D R, Lee G U, Natesan M, Metzger S W, Sheehan P E and Colton R J 1998 *Biosens. Bioelectron.* **13** 731–9
- [55] Miller M M, Prinz G A, Cheng S F and Bounnak S 2002 *Appl. Phys. Lett.* **81** 2211–3
- [56] Ejsing L, Hansen M F and Menon A K 2003 *Euroensors 2003: Proc. 17th European Conf. on Solid-State Transducers (Guimarães, Portugal, Sept. 2003)* pp 1095–8
- [57] Ejsing L, Hansen M F, Menon A K, Ferreira H A, Graham D L and Freitas P P 2004 *Appl. Phys. Lett.* **84** 4729

- [58] Miller M M, Sheehan P E, Edelstein R L, Tamanaha C R, Zhong L, Bounnak S, Whitman L J and Colton R J 2001 *J. Magn. Magn. Mater.* **225** 138
- [59] Rife J C, Miller M M, Sheehan P E, Tamanaha C R, Tondra M and Whitman L J 2003 *Sensors Actuators A* **107** 209
- [60] Schotter J, Kamp P B, Becker A, Puhler A, Brinkmann D, Schepper W, Bruckl H and Reiss G 2002 *IEEE Trans. Magn.* **38** 3365
- [61] Graham D L, Ferreira H, Bernardo J, Freitas P P and Cabral J M S 2002 *J. Appl. Phys.* **91** 7786
- [62] Lagae L, Wirix-Speetjens R, Das J, Graham D L, Ferreira H, Freitas P P, Borghs G and de Boeck J 2002 *J. Appl. Phys.* **91** 7445
- [63] Li G, Joshi V, White R L, Wang S X, Kemp J T, Webb C, Davis R W and Sun S 2003 *J. Appl. Phys.* **93** 7557
- [64] Wood D K, Ni K K, Schmidt D R and Cleland A N 2005 *Sensors Actuators A* **120** 1
- [65] Ferreira H A, Feliciano N, Graham D L, Clarke L A, Amaral M D and Freitas P P 2005 *Appl. Phys. Lett.* **87** 013901
- [66] Anguelouch A, Reich D H, Chien C L and Tondra M 2004 *IEEE Trans. Magn.* **40** 2997
- [67] Shen W, Liu X, Mazumdar D and Xiao G 2005 *Appl. Phys. Lett.* **86** 253901
- [68] Cardoso F A, Ferreira H A, Conde J P, Chu V, Freitas P P, Vidal D, Germano J, Sousa L, Piedade M S, Andrade B and Lemos J M 2006 *J. Appl. Phys.* **99** 08B307
- [69] Ferreira H A, Cardoso F A, Ferreira R, Cardoso S and Freitas P P 2006 *J. Appl. Phys.* **99** 08P105
- [70] Hooge F N 1969 *Phys. Lett. A* **29** 139
- [71] Weissman M B 1988 *Rev. Mod. Phys.* **60** 537
- [72] van de Veerdonk R J M, Belien P J L, Schep K M, Kools J C S, de Nooijer M C, Gijs M A M, Coehoorn R and de Jonge W J M 1997 *J. Appl. Phys.* **82** 6152
- [73] Nowak E R *et al* 1999 *Appl. Phys. Lett.* **74** 600
- [74] Ingvarsson S *et al* 2000 *Phys. Rev. Lett.* **85** 3289
- [75] Park W K, Moodera J S, Taylor J, Tondra M, Daughton J M, Thomas A and Bruckl H 2003 *J. Appl. Phys.* **93** 7020
- [76] Ren C, Liu X, Schrag B D and Xiao G 2004 *Phys. Rev. B* **69** 104405
- [77] Jiang L, Nowak E R, Scott P E, Johnson J, Slaughter J M, Sun J J and Dave R W 2004 *Phys. Rev. B* **69** 054407
- [78] Almeida J M, Ferreira R, Freitas P P, Langer J, Ocker B and Maass W 2006 *J. Appl. Phys.* **99** 08B314
- [79] Ferreira R, Wisniowski P, Freitas P P, Langer J, Ocker B and Maass W 2006 *J. Appl. Phys.* **99** 08K706
- [80] Pannetier M, Fermon C, Le Goff G, Simola J and Kerr E 2004 *Science* **304** 1648
- [81] Edelstein A S, Fischer G A, Pedersen M, Nowak E R, Cheng S F and Nordman C A 2006 *J. Appl. Phys.* **99** 08B317